Stony Brook University

Molecular Dynamic Simulation:

Morphology Study of Organic Photovoltaic Thin Film

A Thesis Presented

by

Di Xu

to

The Graduate School

in Partial Fulfillment of the

Requirements

for the Degree of

Master of Science

in

Materials Science and Engineering

Stony Brook University

May 2012

Stony Brook University

The Graduate School

Di Xu

We, the thesis committee for the above candidate for the

Master of Science degree, hereby recommend

acceptance of this thesis.

Dilip Gersappe – Thesis Advisor
Associate Professor, Materials Science and Engineering

Miriam Rafailovich – Second Reader
Professor, Materials Science and Engineering

Jonathon Sokolov – Third Reader
Professor, Materials Science and Engineering

This thesis is accepted by the Graduate School

Charles Taber
Interim Dean of the Graduate School

Abstract of the Thesis

Molecular Dynamic Simulation:

Morphology Study of Organic Photovoltaic Thin Film

by

Di Xu

Master of Science

in

Material Science and Engineering

Stony Brook University

2012

Engineering heterodyne junction solar cells requires precise positioning of the photoactive polymers and the PCBM conductors such that maximum current reaches the electrodes with minimal resistive scattering. One possible method for accomplishing this may be to use polymer phase segregation in combination with the nanoparticles' natural segregation to the interfaces. In this manner, large-scale devices can be formed using self-assembly methods, rather than fixed methods.

We have used Molecular Dynamics simulation to predict the morphology of polymer blends and determine which combination of factors would yield the optimal cylindrical pattern, which would contact the electrodes, while producing the largest number of interfaces. Secondly, we were also able to determine the conditions that would cause the particles to segregate and template along the interfaces, which would provide direct conductivity to the electrodes. Using thin film and bulk structures and by manipulating particle size, the attraction between the particle and the polymer component, and the amount of filler within the material, we can explore the formation of cheaper, more effective and efficient networks.

Table of Contents

Abstract of the Thesis ..... **ii**

List of Figure ..... **v**

Chapter 1: Introduction **1**

1.1 Conventional P-N Type Solar Cell **1**

1.2 Important Definitions in Solar Cell **4**

1.3 Organic Solar Cell and Principles **6**

1.3.1 Mechanism of Organic Solar Cell 6

1.3.2 Progress in Active Layer Materials 9

1.3.3 Morphology of Organic Solar Cells 11

Chapter 2: Background of Our Study **13**

2.1 Controlling the Morphology of Active Layer **13**

2.2 Novel Column Structure by Self-assembly **14**

2.3 Simulation of OSC Morphology **15**

Chapter 3: Simulation Method **22**

3.1 Molecular Dynamic Simulation Basis **22**

3.4.1 Potential Fields 22

3.4.2 Time-integration Methods 23

3.4.3 Periodic Boundary 23

3.4.4 Neighbor Lists 24

3.2 Simulation Ensemble **24**

3.3 Potential Fields in Molecule Dynamic Simulation **26**

3.4 Other Parameters in Simulation **30**

Chapter 4: Results and Discussion **31**

4.1 Initial State **31**

4.2 Formation of Column Structure **31**

4.3 Impact of δ on Phase Structure **34**

4.4 Nanofiller Confinement **37**

Chapter 5: Conclusion **42**

References **44**

List of Figure

Figure 1. Electron emission from metal surface [4]. 2

Figure 2. Illustration of electron energy band. 3

Figure 3. Electron and hole separation at donor-acceptor interface in planar heterojunction organic solar cell. [10] 7

Figure 4. Illustration of planar and bulk heterojunction formation of active layer in Organic solar cell. [8] 8

Figure 5. Typical structure of layered bulk heterojunction organic solar cell [8]. 9

Figure 6. Illustration of energy levels in a typical Organic Solar Cell [15]..... 10

Figure 7. (a)An ideal carrier-conducting pathway of BHJ. (b)BHJ formed by phase segregation. The carrier-conducting pathways contain bottlenecks and cul-de-sacs. [10]12

Figure 8. Active layer of ordered BHJ portraying lateral phase separated columns of PS and P3HT with PCBM nanoparticles confined to the interface. Illustrated by student researcher. 15

Figure 9. (a) Contour plot of exciton concentrations. (b) Flux, or current, of exciton concentrations. The system morphology possesses a sinusoidal interface with a domain spacing of 12.5 nm and an amplitude variation of ± 20nm. Direction and magnitude of flux is indicated by arrows orientation and size. [26] 16

Figure 10. Typical morphologies generated in two dimensional (100×100) space (a) homophilic chains and (b) heterophilic chains [27]. 17

Figure 11. Comparison of short circuit current density computations (solid line) and experimental data from Ref. [28] (circle line) as function of the blend thickness..... 18

Figure 12. Morphologies with different scales of phase separation, M1 for bilayer, M2 and M3 for blend generated by Ising model, and M4 for checkered structure. Electron and hole conductors (donor and acceptor) are colored with red and blue, respectively [29]. . 19

Figure 13. (a) The morphology generated by Ising model after 9×10^5 time steps. The plot at its bottom shows exciton dissociation efficiency (dotted line), charge collection

efficiency (dashed line), and internal quantum efficiency (solid line). (b) A checkered morphology that designed [30]. 20

Figure 14. (a) Ensemble box of size 32×32 ×16, in all 16384 polymer particles, and with two-layer wall in both side of ensemble. (b) Layer view (x, y plane) of wall particle in FCC (111) manner with 1.00 packing density. (c) Layer view (x, y plane) of polymer particles in FCC (111) manner with 0.81 packing density. 25

Figure 15. Graph of LJ 12-6 potential. rm is the distance with minimum potential [33]. 27

Figure 16. Plot of LJ potential to distant with different value of δ, from 0.1 to 1 28

Figure 17. Illustration of distance-shift between PCBM and other particles. The solid sphere represent PCBM hard sphere, dashed circle represent other particles. PCBM sphere has radius of Δ=0.5, which is about four times bigger in volume than PS and PCBM particles. And the weight of PCBM was set 3 in contrast to 1 for PS and P3HT. 29

Figure 18. Random distributed P3HT chains (blue color) in simulation box. Walls are pink color one, PS was made transparent, and there is no PCBM in this system. 31

Figure 19. Structures of P3HT phase at different stage. (a) Structure after 1 million steps. (b) Structure after 2 million steps. (c) Structure after 5 million steps. (d) and (e) are Structure after 8 million steps with different angle of view. 32

Figure 20. (a) TEM picture of PS:P3HT:PCBM 1:1:1 thin film, top view. (b) TEM picture of the cross-section. 34

Figure 21. Structures of systems with different δ value, after 8 million simulation steps. 35

Figure 22. Structures evolved with time from (a) 8 million steps to (b) 16 million steps. 36

Figure 23. Number of P3HT particles at interface along with time steps. In all 3456 P3HT particles were in the simulation box. 37

Figure 24. Position of PCBM (black) and structure of P3HT (blue) in simulation systems after 5 million steps. (a) δP3HT:PS=0.55. (b) δP3HT:PS=0.65. (c) δP3HT:PS=0.75 38

Figure 25. Number of PCBM at interface alone with simulation time for different degree of immiscibility between PS and P3HT. 39

Figure 26. Distribution of PCBM in P3HT:PS bilayer after 3 million steps. (PS was made transparent) a. δPCBM:PS=1.0 (neutral); b. δPCBM:PS=0.95; c. δPCBM:PS=0.90; δPCBM:PS=0.80. 40

Figure 27. Systems with different number of PCBM particles (after 8 million steps). From a to d, number of PCBM equal 64, 256, 512, and 1024 respectively..... 41

Acknowledgments

I would like to thank to my advisor Dilip Gersappe in Stony Brook University for his help with the research and kindly provide me equipment that needed for simulation. And professor Miriam Rafailovich, she gave me reference on the Solar Cell studies.

Other members in our research group also gave me a lot of help. Joseph Ortiz and Ning Sun. I learned a lot from the fruitful discussions we had.

At last, thanks to parent for supporting my study. And my fiancé Zexi Han, she is always supportive.

Chapter 1: Introduction

Human have been trying to convert sunlight into capable energy forms early in history. e.g. such as using it to dry wet clothes. In1839, Edmond Becquerel discovered the photoelectric effect [1], which allowed another means by which humans could capture solar energy. With increasing public concerns on the upcoming energy crisis and on pollution issues related to global warming, research in utilizing the potential of solar cells has drawn intense attention since late last century.

1.1 Conventional P-N Type Solar Cell

The prevailing solar cell products presently on the market are mostly based on silicon wafers, and are considered a "first generation" solar cell [2]. This conventional p-n type solar cell was first invented at Bell lab in 1954 [3]. However, the theory can be traced back much earlier in history. As for now, the principles of conventional solar cell have been well understood.

The photovoltaic process can be fundamentally explained from the energy that light has carries. Photons carry different degree of energy that depends on the frequency, or color (wave length). Einstein in 1905 proved in his experiments that blue or ultraviolet light could provide enough energy for electrons to escape completely from the surface of metal, figure 1 [4].

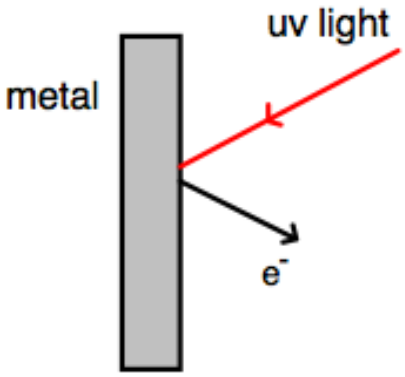

Figure 1. Electron emission from metal surface [4].

Photon excited electrons were also observed in semiconductors. In principle, electrons are tightly bounded to solids in their ground state (valence band). It is a stable state in which movements of electrons were strictly limited. When incident light brings photons, the carried energy will instigate some of the electrons to jump to a higher energy level, which is called conducting band, see illustration in figure 2. This phenomena is called the photoelectric effect, it was explained by the fact that electrons adsorb the energy carried by photon and overcome the barrier between valence band and conducting band, thus only photons with energy higher than the band gap would count for this effect.

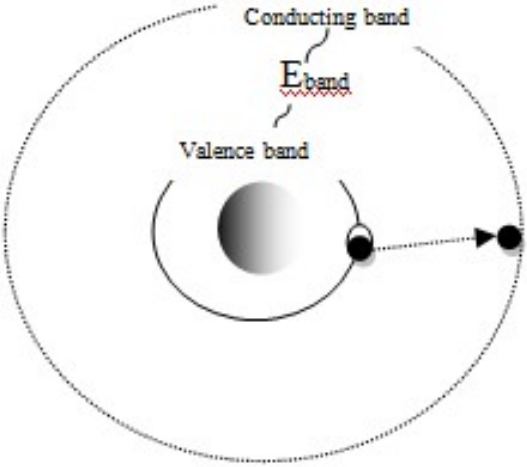

Figure 2. Illustration of electron energy band.

Electrons at conducting band were "freed" and could move from its original lattice site, if electrons could reach electrode contacts, electric current would be generated. However, excited electrons mostly relaxed back to its ground state and the energy was wasted. In order to capture the excited electron, a driving force must be provided to prevent the electron from relaxing. In semiconductor solar cells, this was achieved by constructing a p-n junction. N-type semiconductor was doped with impurities to make it have an excess of electrons while P type semiconductor was made have an excess of holes, or in other word a lack of electrons. In such a structure, an excited electron when generated in P type semiconductor phase would lead to a potential difference and finally drive electron and holes through an external load.

P-N type solar cell was discovered in 1950's following the development of silicon electronics. When Chapin and Fuller, first invented the silicon solar cell in1954, their devices was reported to have a conversion efficiency of 6%, which is six times larger

than the previous record at that time. This great improvement was mainly due to the better rectifying action of p-n junction structure. In the following decade, p-n type solar cell became the mainstream of solar cell research. Silicon based p-n type solar cell dominate both the research and market world by taking advantage of the more matured silicon technology.

In the past 15 years, this p-n based device has stepped into its second generation that is from silicon wafer to thin-film technology [2]. This evolution has brought significant improvement in conversion efficiency, in 1980, the first thin-film cell developed in University of Delaware brought the conversion efficiency to 10%. In 1993, a landmark of 30% efficiency was achieved. In 2006, the 40% efficient barrier was broken [5].

1.2 Important Definitions in Solar Cell

There are some properties and definitions that are important when studying solar cell [4]. As the generated current is depended on incident light and device itself, we need an internal parameter that can bridge incident light and device characteristics. Quantum Efficient (QE) was then introduced. QE is defined as the probability that a photon with energy E could successfully deliver an electron to the external circuit. It was a function of E but independent of incident light, the factors affected QE(E) includes the ability of the material to adsorb photons, the efficiency of the device in charge separation and collection. QE (E) correlated with photon-current density via the manner

$$J_{SC} = q \int b_s(E) QE(E) dE$$

where $b_s(E)$ is the incident spectral photon flux density.

When solar cell was exposed to a load, a current will generated that act opposite to the photon-current. This reverse current is called dark current. In most cases, the dark current has the form

$$J_{dark}(V) = J_0(e^{\frac{qv}{k_b T}} - 1)$$

J_0 in the equation is constant, K_b is Boltzmann constant, and T is temperature in Kelvin degree. Net current density was thus

$$J(V) = J_{sc} - J_{dark}(V)$$

When two electrode contacts are isolated, the potential difference between two terminals is the open circuit voltage V_{oc}

$$V_{oc} = \frac{kT}{q} \ln\left(\frac{J_{sc}}{J_0} + 1\right)$$

The output power (energy) of solar cell will reaches maximum at certain value of J and V since P = JV, this point is called maximum power point, and the corresponding J and V are named J_m and V_m. the Fill Factor was defined as

$$FF = \frac{J_m V_m}{J_{sc} V_{oc}}$$

Efficiency η of the cell is the percentage of incident energy that solar cell could convert into electric, and has the form

$$\eta = \frac{J_m V_m}{P_s} = \frac{J_{sc} V_{oc} FF}{P_s}$$

These parameters are the key factors that measure the performance of a solar cell device and are usually used to test new devices and architectures.

1.3 Organic Solar Cell and Principles

Despite the high conversion efficiency, conventional solar cells suffer from high manufacturing cost. As reports indicate, for silicon wafer industries, material costs accounted for 70% of the total [6]. Comparatively, Organic solar cell (OSC) has became a promising cost-effective alternative to silicon-based one. This is because easily processed polymers have served as main material in most OSC's. At the same time, organic solar cells have advantages like light weight and flexibility which could meet the growing need of portable and sustainable energy source for new technologies.

1.3.1 Mechanism of Organic Solar Cell

The mechanism of an organic solar cell is generally accepted as consisting of two steps, which is exciton generation and charge separation [7]. This can further be divided into 1) Adsorption of photons, 2) Exciton generation, 3) Exciton separation and 4) Charge collection, for solar cell devices [5]. At the photogeneration step, the photovoltaic part adsorb photons and convert them to electron-hole pairs. Then, at the separation step, electron and hole are separated, following the internal electric field, they drift to different electrodes. However, there exists a big difference in principle between organic solar cell and conventional semiconductor based solar cell, largely at electron-hole separation steps.

It is worth to note, the photovoltaic material in organic solar cell alone could produce photovoltaic current [8]. But, the excitons produced in OSC are tightly bonded. In such case, the excitons have to remain intact until reach an electrode or reach an interface of Donor and Acceptor, in the case of a heterojunction device. Because the

limitation of exciton diffusion range (≤20nm [9]), thin film heterojunction OSC with donor-acceptor materials has proved to have better performance. The exciton separation could be depicted by figure 3 for planar heterojunction OSC. However, in planar heterojunctions, large volume of excitons that located far from interface are trapped and contribute nothing to electric flow. Yu et al. and Halls et al. addressed this problem by proposed polymer/polymer mixing as active layer that forms an interpenetrating network, which recognized as Bulk Heterojunction (BHJ)[11][12]. Figure 4 demonstrates the different morphologies of a planar and BHJ solar cell. The exciton diffusion distance was significantly reduced in BHJ formation and efficiency has been brought to over 3% in P3HT based BHJ solar cell [13][14].

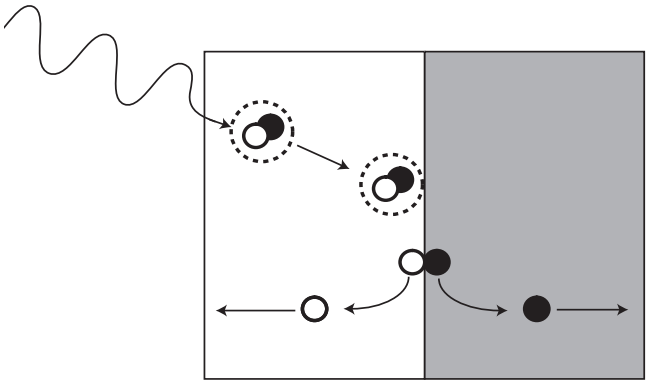

Figure 3. Electron and hole separation at donor-acceptor interface in planar heterojunction organic solar cell. [10]

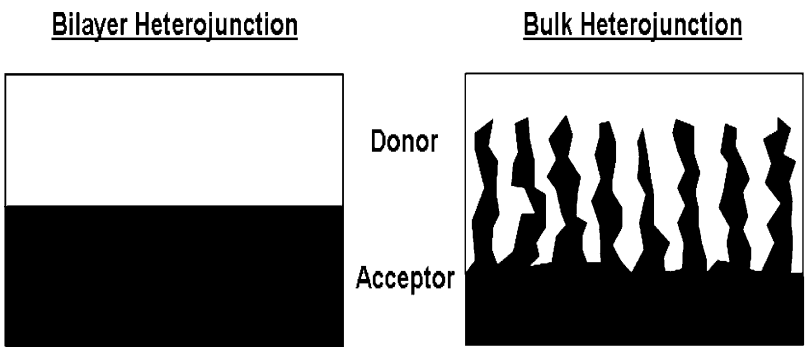

Figure 4. Illustration of planar and bulk heterojunction formation of active layer in Organic solar cell. [8]

While the conversion efficiency of OSC have seen significant improvements, the efficiency remains small compared to conventional solar cell. Efforts have been made to improve OSC conversion efficiency. On the one hand, scientists improved structure of OSC, such as making tandem OSC, introducing PEDOT-PSS as hole transporter. The structure of a typical layered OSC is shown in figure 5. On the other hand, scientists focused on the BHJ active layer of OSC. A large number of combinations of acceptor-donor material have been investigated.

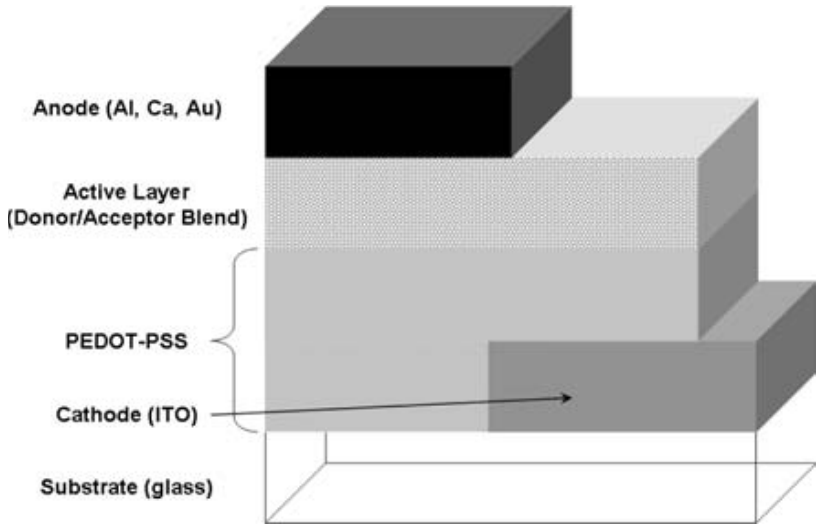

Figure 5. Typical structure of layered bulk heterojunction organic solar cell [8].

1.3.2 Progress in Active Layer Materials

A great deal of research has been made in donor and acceptor materials aiming to improve the conversion efficiency. In principle, materials with a delocalized π electron system has the potential to be used as active layer materials since it can absorb light photons to generate excitons and can transport charge carriers. But to achieve better performance, there are some guidelines in selecting or modifying donor and acceptor materials. Band gap is an important factor that affects the performance of OSC, the same as described for semiconductor, as the photovoltaic materials in OSC can only adsorb photons that carry energies larger than its energy band gap. In OSC, this energy gap is between Highest Occupied Molecular Orbital (HOMO) and Lowest Occupied Molecular Orbital (LUMO), see figure 6 [15]. The maximum short circuit current of OSC device is thus determined by the smaller band gap of donor or acceptor. The open circuit Voltage

output is limited by the gap between HOMO orbit of donor and LUMO orbit of acceptor. Studies also show that the offset of LUMO and HOMO (ΔE_{lumo} and ΔE_{homo}) has to reach a significant level in order to get desirable efficiency [16]. In efforts to achieve higher conversion efficiency, all above factors have to be taken into account.

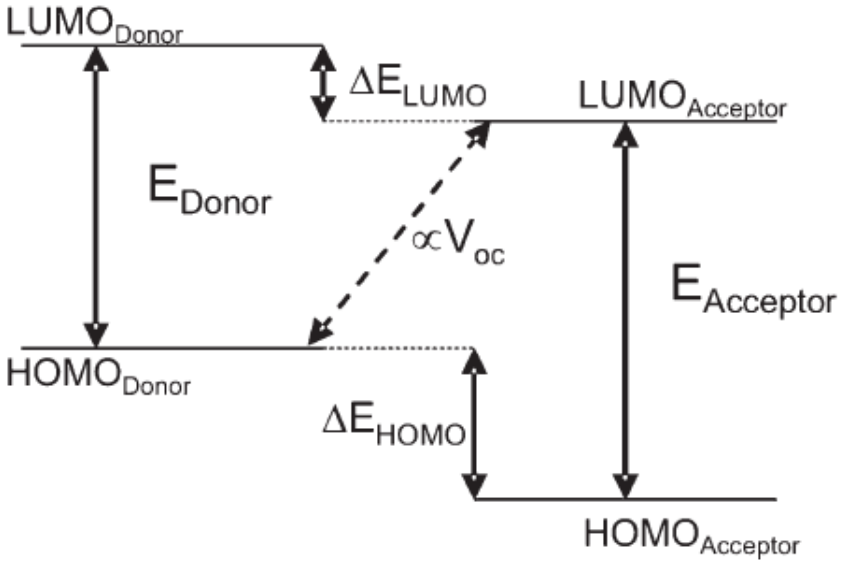

Figure 6. Illustration of energy levels in a typical Organic Solar Cell [15]

Yu and etc. in 1995 [11] used MEH-PPV: PCBM blends as active layer material and efficiency of nearly 1% percent was discovered, it was a record for OSC at that time. But soon afterward, P3HT: PCBM proved to have superior properties, and even until today, it is regarded as the most promising materials for OSC. Despite the fact that most lab OSC was based on P3HT: PCBM, progress has been made in seeking higher performance materials. As reviewed by Gillers, donor materials have four types, which are Fluorene-based copolymers, Carbazole-based copolymers, Cyclopentadithiophene-based Copolymers and Metallated Conjugated Polymers [15]. The driving force to find

P3HT alternatives is mainly due to the poor overlapping between P3HT adsorption spectrum and solar spectrum. In an optimal situation, P3HT could at most adsorb 22.4% of the photons arrives earth surface [17]. Therefore, donor with smaller band gap will provide much larger space for improvement. Among these alternatives, Poly[2,1,3-benzothiadiazole-4,7-diyl[4,4-bis(2-ethylhexyl)-4H-cyclopenta[2,1-b:3,4-b']dithiophene-2,6-diyl]] (PCPDTBT) with a band gap as small as 1.45 eV showed large potential. Zhu and et al. observed efficiency of 3.5% in PCPDTBT: PCBM device [18]. At the same time, acceptor materials were also investigated since current widely used PCBM materials contribute little to photon adsorption. Conjugated polymers, fullerenes, carbon nanotubes, graphene, and etc. have investigated. But in compromise of charge mobility and adsorption, PC(60)BM and PC(70)BM were still considered as most efficient acceptor material so far.

1.3.3 Morphology of Organic Solar Cells

To further enhance the conversion efficiency of OSC, we need to develop a clear understanding of the relation between morphology and efficiency. It is now understood that due to the diffusion path of excitons, a large interfacial area for electron-holes separation and a continues pathway (figure 7.a) for electron and hole transport is required for high performance [19]. The development of Bulk Heterojunction active layer has reduced the exciton diffusion distance and extended the interfacial area. However, the random nano-scale formation impedes the transportation of electron and hole. Like in figure 7.b, in this tortuous structure, a significant portion of electrons are blocked at the bottleneck and the contorted travel route increase the diffusion distance.

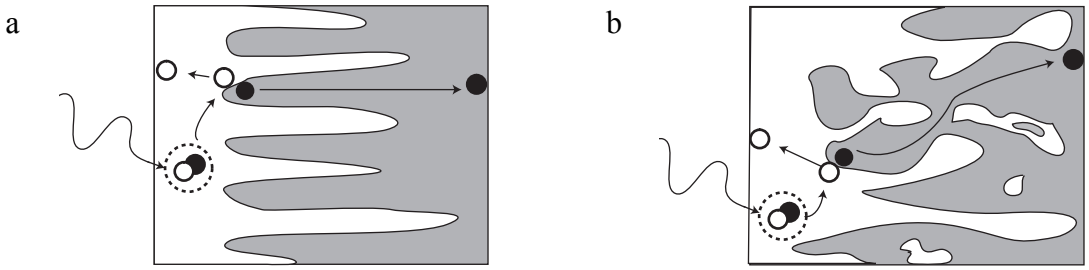

Figure 7. (a)An ideal carrier-conducting pathway of BHJ. (b)BHJ formed by phase segregation. The carrier-conducting pathways contain bottlenecks and cul-de-sacs. [10]

Chapter 2: Background of Our Study

2.1 Controlling the Morphology of Active Layer

Surface patterning and new deposition technique have been used to get an organized OSC structure [10][20][21]. However, most BHJ layer is deposited from polymer solution. The morphology is affected by thermodynamic parameters, like the Flory-Huggins parameter, and kinetic effects, like solvent evaporation rate. Thus, influence of solvent, compound ratio, annealing, and etc., are important parameters in morphology control.

There are some remarkable studies about control the morphology of active layer to enhance photovoltaic performs. Most of high conversion efficiency P3HT: PCBM devices has been annealed to enhance the performance, but there lacks of through study about the effect of annealing, Yang and et al. revealed that annealing could increase the crystallization of both P3HT and PCBM, especially P3HT, while the interface of P3HT: PCBM will not decrease much [22]. It explains the improvement in the efficiency after annealing. J. PEET and et al. found by adding small concentration of alkanethiol in P3HT: PCBM solution, the phase separation can be modified. If same method were used in PCPDTBT: PC(71)BM based device, efficiency as high as 5.8% can be reached [23]. Mariano and et al. try to find the commons among the nowadays widely used morphology control technique, such as solution selection, casting technique and post treatments. They used methods including Raman spectrum, Optical microscopic and AFM to show that all control technique tended to form similar arrangement of

components, which is a laterally and vertically phase-separated blend of crystallized P3HT and PCBM [24].

2.2 Novel Column Structure by Self-assembly

Self-assembly is a process in which spontaneously assemble into a stable morphology. This technique attract interests as it provide a alternative method for controlled fabrication of nanometer scale objects while existing fabrication technique suffer from disadvantages including size restrictions and general paucity of applicable materials [25]. Self-assembly was introduced to OSC fabrication because of the polymer blend nature of OSC active layer and as the existing fabrication mechanisms for an organized structure are expensive and time consuming. Indeed, a Bulk Heterojunction structure is exactly one typical result of self-assemble, the question left is how to manipulate this process well to get the structure that we want.

Miriam Rafailovich and her students recently found that by introducing a non-conducting component (PS) into OSC active layer could lead to a self-assembled column structure between two electrode, the expected structure is like figure 8. This ordered structure provides a continuous pathway for exciton diffusion and the solution process was cost effective. Study of this innovative method is promising.

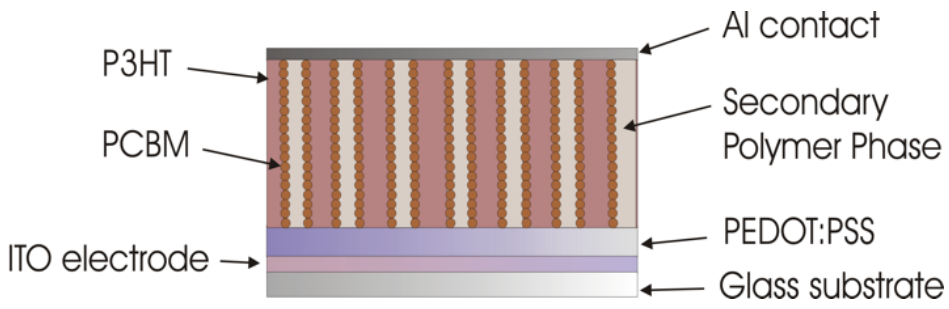

Figure 8. Active layer of ordered BHJ portraying lateral phase separated columns of PS and P3HT with PCBM nanoparticles confined to the interface. Illustrated by student researcher.

2.3 Simulation of OSC Morphology

As depicted above, the morphology of OSC active layer plays a crucial role in the photovoltaic process and is expected to have biggest impact to conversion efficiency. Traditional analysis techniques like TEM, SEM, and SPM are mainly limited in 2-dimensional observation, however the OSC performance are strongly depends on 3-dimension organization. A local resolution in three dimensions is required to understand bulk heterojunction structure and charge carrier transports better [22]. At the same time, for a self-assembly process, the underlying theory is not clear, the results of self-assembly were largely based on prediction and proved later by experiments.

Simulations have been a powerful tool to study the morphology of the OSC active layer. The growth of fast processing, speeds and large scale parallelism also enabled simulations to model large system size and to study optimum parameter sets. Until now, many simulations have been performed in order to explore the relation between morphology and OSC performance.

Gavin A Buxton and Nigel Clarke used a 2-D drift-diffusion model to investigate the transient behavior of electron, hole and exciton concentrations in heterogeneous

bilayer device with distinct donor and acceptor phases [26]. In their model, the interface was built as variant sinusoidal structure to correlate device performance with internal structure. The concentration and flux of photogenerated excitons is shown in figure 9. It was observed that exciton concentration decreased at donor-acceptor interface, which is due to exciton dissociation. Systems with different sinusoidal domain, concentration and flux of electron and holes were also studied in their work. Their results provide insights of internal charge particle distribution and transportation.

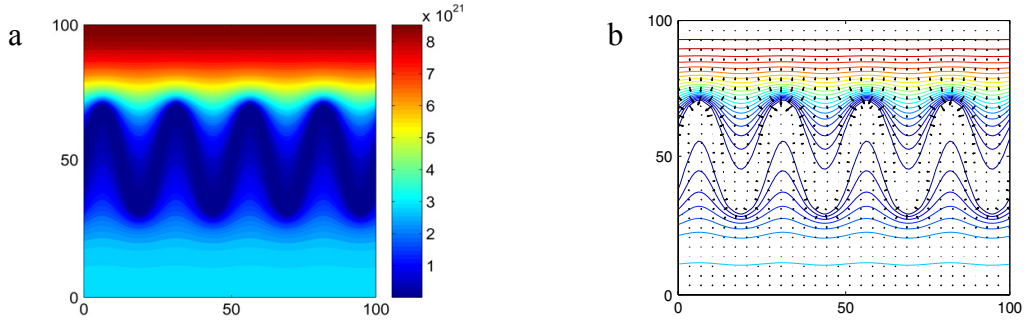

Figure 9. (a) Contour plot of exciton concentrations. (b) Flux, or current, of exciton concentrations. The system morphology possesses a sinusoidal interface with a domain spacing of 12.5 nm and an amplitude variation of ± 20nm. Direction and magnitude of flux is indicated by arrows orientation and size. [26]

Jarvist M. Frost, et al., used Monte Carlo algorithms to produce a 2-D structure of Donor-Acceptor blends. By controlling donor and acceptor polymer chains as mutually attractive or mutually repulsive, they got aggregation of chains into large domains for homophilic chains and dispersion of chains into isolated strands for heterophilic chains, like in figure 10. They then applied these morphologies in simulations of photocurrent quantum efficiency for donor –acceptor blend photodiodes. The results showed the effects of morphology on charge pair generation and recombination compete with the effect on transport [27].

Figure 10. Typical morphologies generated in two dimensional (100×100) space (a) homophilic chains and (b) heterophilic chains [27].

Florent Monestier and et al., investigated the short-circuit current density of P3HT:PCBM based OSC by using their model to simulate charge transport [28]. Exciton generation rate is used as input data for their model, and short circuit current density was calculated from charge densities at steady state. Their work reveals the thickness dependence of short-circuit current of P3HT:PCBM thin film. Figure 11.

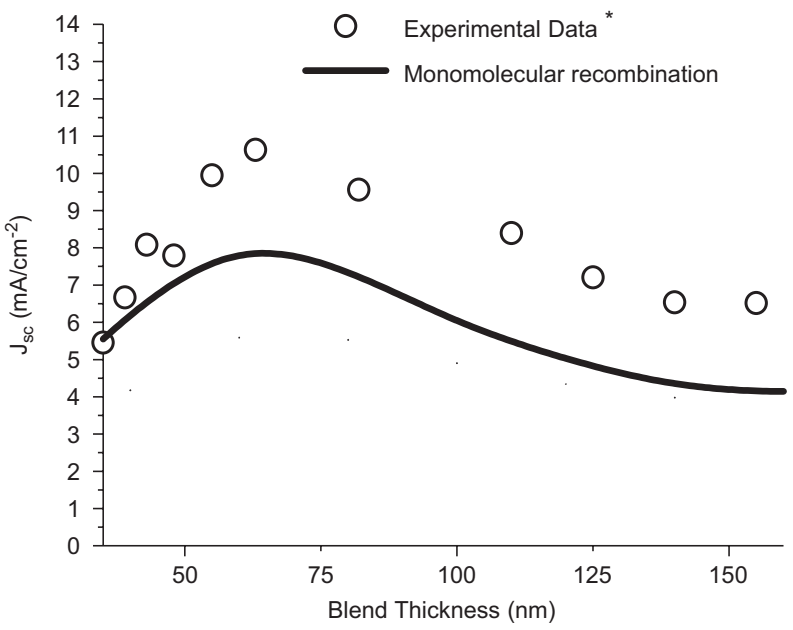

Figure 11. Comparison of short circuit current density computations (solid line) and experimental data from Ref. [28] (circle line) as function of the blend thickness

Lingyi Meng, et al., investigated the relation of morphology and performance of donor-acceptor by using dynamic Monte Carlo simulations [29]. In their model diffusion, exciton dissociation, the drift, the injection from electrodes, and the collection of charge carries by electrode have been taken into account. With four morphologies they investigated, in figure 12. They found blend system M3, M4 can reach power conversion efficiency as high as 2.2% and 2.7% respectively. They also expected 5% conversion efficiency could be achieved with optimal charge mobility and optimal thin film morphology.

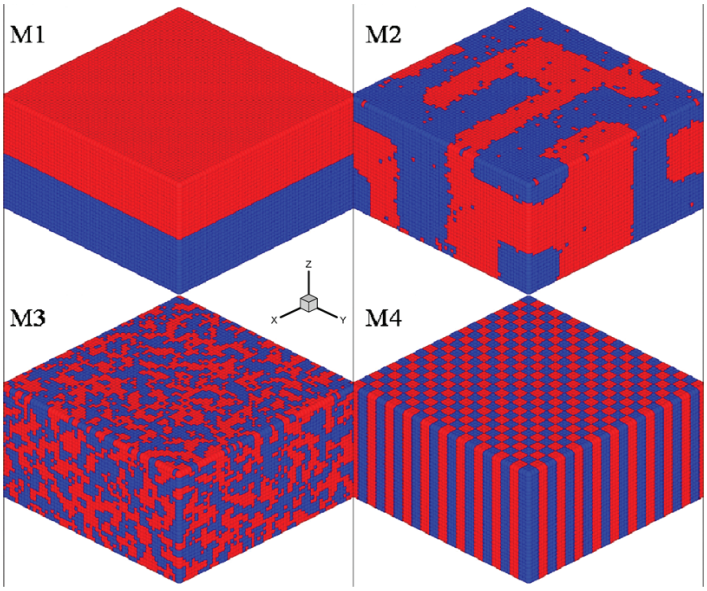

Figure 12. Morphologies with different scales of phase separation, M1 for bilayer, M2 and M3 for blend generated by Ising model, and M4 for checkered structure. Electron and hole conductors (donor and acceptor) are colored with red and blue, respectively [29].

Peter K. Watkins and et al., have did related work earlier in 2005 [30]. They specifically studied impact of morphology on internal quantum efficiency (IQE) of bulk heterojunction solar cell. They found IQE is strongly sensitive to scale of phase separation in morphology. IQE reached peak at an intermediate scale phase separation, shown in figure 13. And an ordered morphology exhibits a peak IQE 1.5 times higher.

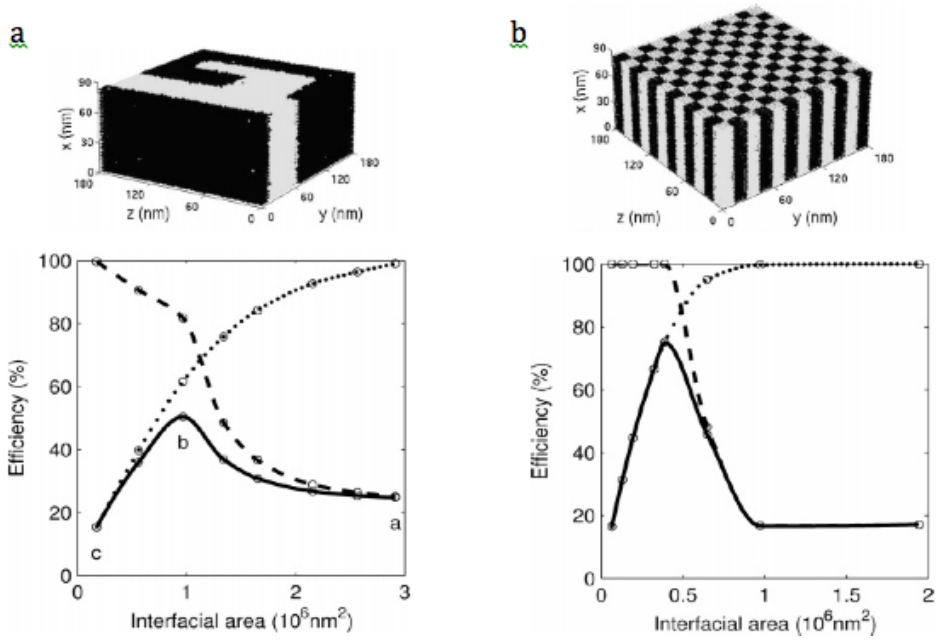

Figure 13. (a) The morphology generated by Ising model after 9×10^5 time steps. The plot at its bottom shows exciton dissociation efficiency (dotted line), charge collection efficiency (dashed line), and internal quantum efficiency (solid line). (b) A checkered morphology that designed [30].

While most of these works mentioned were tended to construct connection of OSC active layer morphology and OSC performance. Simulation studies about morphology prediction can be found in the thin film field. Because of the OSC layer are thin film structures and are deposited from polymer blend. ex. Harkravarth Ayyngar and et al., used Molecular Dynamics simulation to study the influence of free surface on morphology of thin films and bulk melts [31]. Pramod Kulkarni and et al. used Brownian Dynamic Simulation to predict morphology of Nanoparticle Deposits in the presence of interparticle interactions [32].

The purpose of our work is to study the morphology of columnar structure of P3HT:PCBM which is formed by introducing PS as non-conductive third party, as

mentioned before. We have used Molecular Dynamics simulation to predict the column structure. We also studied the impacts of parameters to the morphology and tried to find optimal parameter combination.

Chapter 3: Simulation Method

3.1 Molecular Dynamic Simulation Basis

Molecule Dynamic simulation is a numerical computational method that predicts trajectories of atoms or other particles inside physical ensemble. By calculate interaction force between particles and using newton motion equations, acceleration value could be achieved. When the calculation was launched every micro-time steps, the discrete results could present an accurate prediction of particle movements. Combined with statistic methods, MD could help people understand physical behaviors, like thermodynamic, of materials. It has now become an important tool in materials researches and materials design.

3.4.1 Potential Fields

In MD simulation, newton mechanics are the underlying calculation rules, all interaction forces are derived from potential and distance. Potentials in an MD simulation can usually divide to bonded potential and non-bonded potential.

When considering non-bonded potential, there is variety of physical models. Some potential equations only include pair interaction while others may consider many body effects. Potential equations that describe Van der Waals force are usually used, such as Lenard-Jones 12-6 equation. If electrostatic charges are present, coulombic force and related potential equations should be included in the simulation. However, it should be noted that Van der Waals force falls significantly when distance increased, so a cut-off

distance is always used to save calculation time waste. But coulombic force is a long-range force, thus only a much larger cut-off value could ensure the precision of model.

If modeled system has chemically bonded particles, bonded force must be calculated. A great numbers of physical models have been developed to model chemical bond potential so far, such like AMBER, CHARMM, and FENE. Selection of bond potential model should be depending on the simulation system and considering the economics in calculation.

3.4.2 Time-integration Methods

A lot of algorithms provide time integration of newton motion equations. Among them are Verlet Algorithm and Leap-frog Algorithm. Both of them are essentially predictor method that the molecular coordinates are derived from either current or previous steps. Predictor-Corrector algorithm is a little different as it added a corrector step.

Due to the nature of numerical methods that involved in MD, say the discrete time. The result, unlike analytical one, will however deviate from the reality in long time scale despite that smaller unit time step can improve precision by sacrificing speed.

3.4.3 Periodic Boundary

Compared to real system with vastly numbers of particles, a simulation sample usually has very small size. A periodic boundary is what usually used in all kinds of simulations to minimize the error from surface effect. The idea of a periodic boundary in MD is similar as to replicate this simulation system in the periodic direction. Thus when

particle moves outside the boundary, will reenter in opposite side. And particles also interact across the boundary.

3.4.4 Neighbor Lists

A cut-off distance could save calculation significantly. However, it requires updates of distance every calculation step to judge if pairs is within the cut-off range. This when in a large system, costs a lot of calculation power to cover every pair of particles. A neighbors list of each particle is constructed by setting another pairwise range that larger than cut-off. Particles in that range are considered as "candidates" for the cut-off judgment. In selecting a proper neighbor range, we can update the neighbor info every multiple simulation steps. This avoids unnecessary calculation waste and has been widely accepted in MD simulations.

3.2 Simulation Ensemble

We performed Molecular Dynamic (MD) simulation of a rectangle ensemble box. Quantities in simulation are set unitless based on Lennard-Jones standard. The ensemble was initially constructed with size 32×32 ×16 in X, Y, Z direction respectively, and X, Y direction were set as periodic boundary, figure 14a. In Z direction at top and bottom, a two-layer wall was constructed at both sides. The wall particles were arranged in a Close-Packed FCC (111) plane, the pack density was set 1.00, figure 14b. The top wall was set shrinkable in order to achieve fix pressure equilibrium. Polymer particles were also arranged in FCC (111) manner but with pack density 0.81, figure 14c.

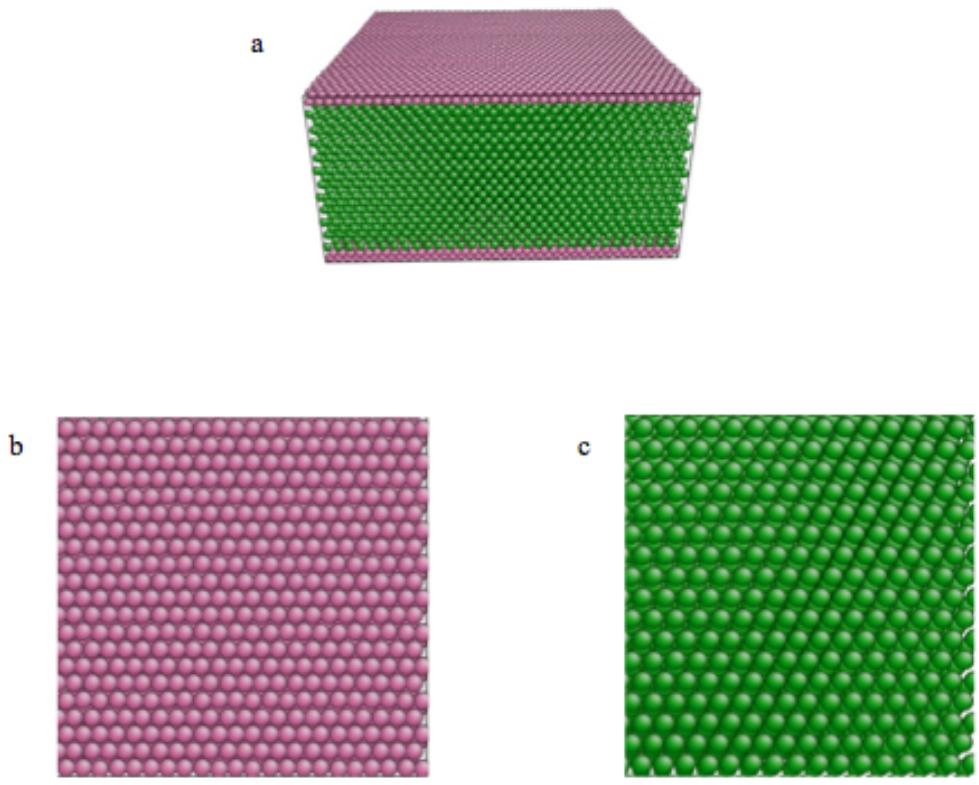

Figure 14. (a) Ensemble box of size 32×32 ×16, in all 16384 polymer particles, and with two-layer wall in both side of ensemble. (b) Layer view (x, y plane) of wall particle in FCC (111) manner with 1.00 packing density. (c) Layer view (x, y plane) of polymer particles in FCC (111) manner with 0.81 packing density.

Polymers in the systems has 32 monomers in each chain, in all 512 chains (PS) were initially in the system. After equilibrium, a second phase particles (P3HT) and filler particles (PCBM) were manually put into the systems by converting a fraction of the PS chains at random. Thus, the number of particles in the system remains the same through all simulation process. However, the system size was evolved through simulation, since we allow top wall to be shrinkable.

It should be noted that though we are trying to relate our model to PS:P3HT:PCBM thin film system, the works are exactly general problem of a heterophilic blend with nanofillers distributed in it.

3.3 Potential Fields in Molecule Dynamic Simulation

Particles in our simulation were interacted via Lenard-Jones (LJ) potential, classic 12-6 potential in equation (1). This LJ equation is great approximation of interaction between pair of neutral atoms and molecules.

$$V(r) = 4\varepsilon\left(\left(\frac{\sigma}{r}\right)^{12} - \left(\frac{\sigma}{r}\right)^{6}\right) \tag{1}$$

In the equation, ε is the depth of the potential well, σ is the finite distance at which the inter-particle potential is zero, which is so called balance position, r is the distance between two particles. First part of the equation, with index 12, describes the repulsion between particles. Second part, with index 6, describes the attraction between particles. LJ potential to pair distance was plotted in figure 15. Repulsion force increased significantly when pair distance is smaller than 1, and attraction force tended to link two pair from separating too far away.

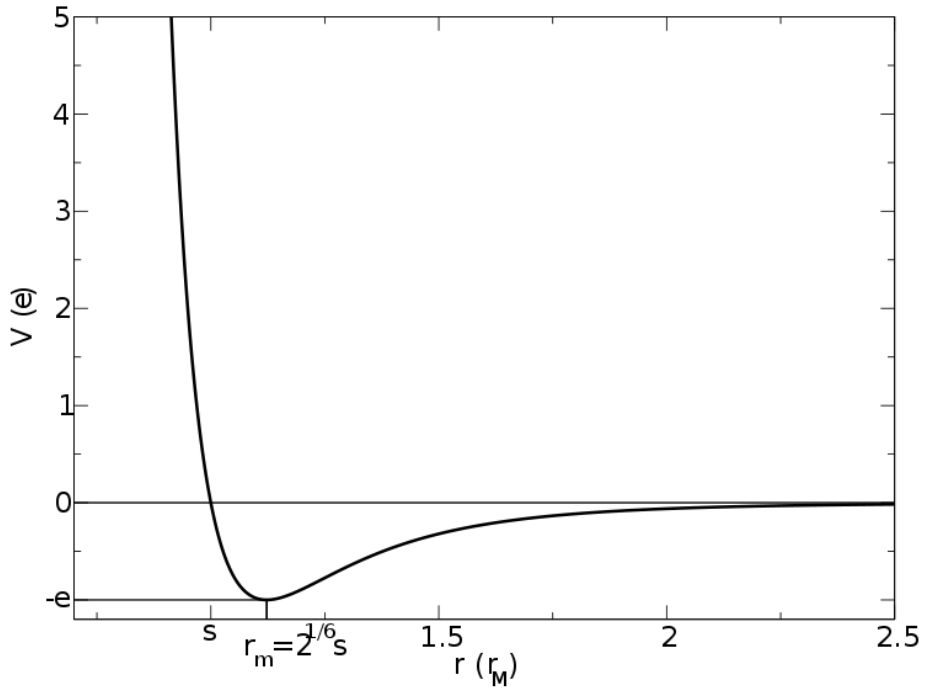

Figure 15. Graph of LJ 12-6 potential. rm is the distance with minimum potential [33].

Mostly, immiscibility of two polymer phases was defined by Flory-Huggins theory, which explained phase separation according to thermodynamic basis. In our simulation, we introduced parameter δ in front of attraction part, equation (2), in order to consider phase separation via particle interaction rather than consider global thermodynamics. When δ is set less than 1, the attraction force was modified and the pair tended to perform immiscible behavior. In our work, different δ value was tested to simulate different degree of immiscibility. The effects of δ on LJ potential could be seen in figure 16.

$$V(r) = 4\varepsilon\left(\left(\frac{\sigma}{r}\right)^{12} - \delta\left(\frac{\sigma}{r}\right)^{6}\right) \qquad (2)$$

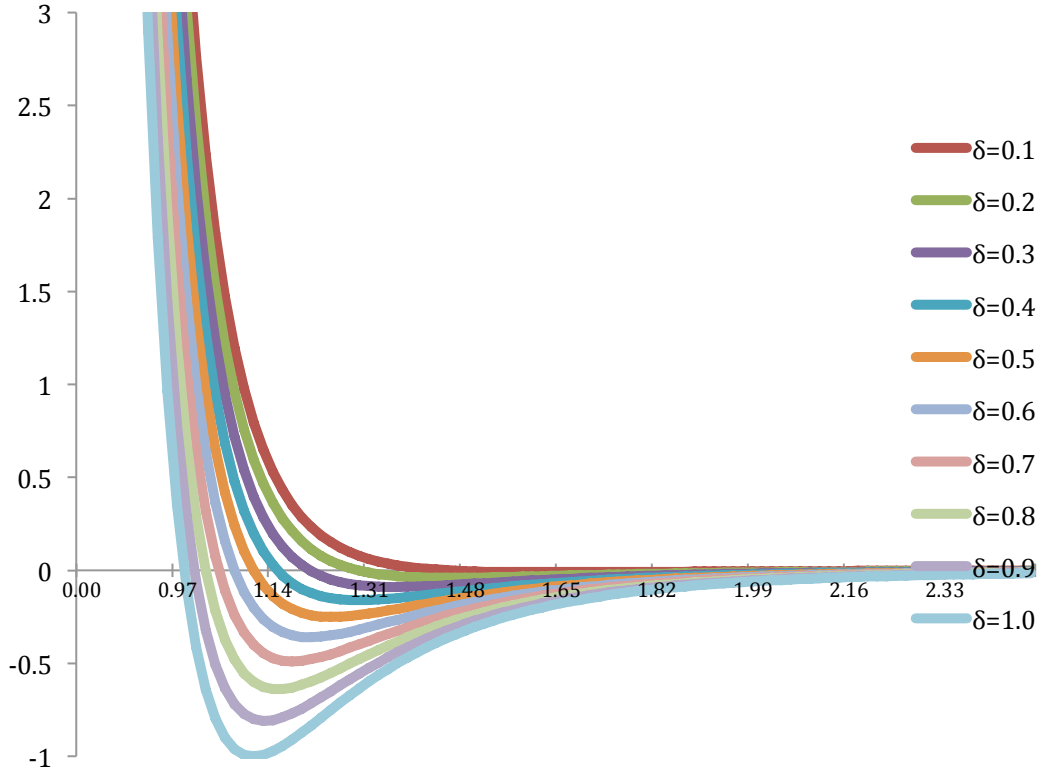

Figure 16. Plot of LJ potential to distant with different value of δ, from 0.1 to 1

$$V_{\text{truncated LJ}} = V(r) - V(r_{\text{cutoff}}) \ (r > r_c) \qquad (3)$$

A truncated LJ equation, (3), was used in simulation rather than the origin (1) equation. This method is widely used in MD studies. We set cut-off distance in our simulation at value 2.5σ, which means pairs with distance farther than 2.5σ will not be taken into account. It can be calculated, at r=2.5σ, the potential was

$V(r = rc = 2.5\sigma) = 4\varepsilon\left[\left(\frac{\sigma}{2.5\sigma}\right)^{12} - \left(\frac{\sigma}{2.5\sigma}\right)^{6}\right] \approx -0.0163\varepsilon$, Which is a low level that could be reasonably neglected. This cut-off method could significantly decrease the computational cost.

Since we introduced PCBM into the system as nano-filler and consider it as a hard sphere, the distance between PCBM and other species of particles should be shifted by a value Δ that equals the radius of PCBM hard sphere, see figure 17. The LJ equation was then changed to the form (4), with Δ=0.5 for PCBM, Δ=0 for other particles.

$$V(r) = 4\varepsilon\left(\left(\frac{\sigma}{r-\Delta}\right)^{12} - \left(\frac{\sigma}{r-\Delta}\right)^{6}\right) \qquad (4)$$

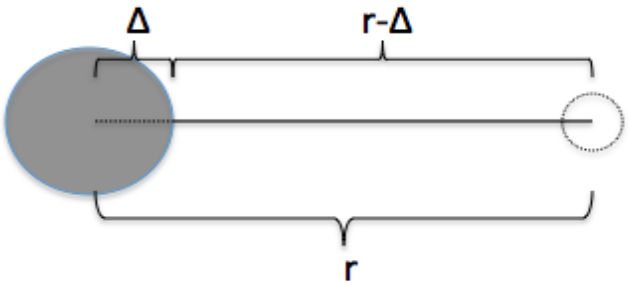

Figure 17. Illustration of distance-shift between PCBM and other particles. The solid sphere represent PCBM hard sphere, dashed circle represent other particles. PCBM sphere has radius of Δ=0.5, which is about four times bigger in volume than PS and PCBM particles. And the weight of PCBM was set 3 in contrast to 1 for PS and P3HT.

After all modification, the LJ potential used in our simulation has the final form

$$V(r) = 4\varepsilon\left(\left(\frac{\sigma}{r-\Delta}\right)^{12} - \delta\left(\frac{\sigma}{r-\Delta}\right)^{6}\right) - (-0.0163\varepsilon) \qquad (5)$$

For those chemically bonded particles, we used Finitely Extensible nonlinear elastic (FENE) potential to maintain them connected together, see equation (6). Kremer and et al. has used this equation in their MD simulation [34]. K is the bond spring

constant and was set 30 in our simulation. R_0 is finitely extensibility and was set 1.5 σ.

$$V_{CH}(r) = -\frac{1}{2} K R_0^2 \ln\left(1 - \left(\frac{r}{R_0}\right)^2\right) \quad (6)$$

3.4 Other Parameters in Simulation

The whole system was considered at a fixed temperature. This was controlled by Langevin thermostat, which consider particles under heat bath and was continuously bumped by solvent particles. Time integration was via fifth order predictor-corrector algorithms, which was proposed by Gear in his book [35]. The time step in our simulation was set 0.005. Most parameters, their meaning and values can be found in table 1.

ε	Lenard Jones potential well	Δ	Radius of PCBM hard sphere
σ	Finite distance at which the inter-particle potential is zero	r_c	Cut off distance, beyond which interaction are not considered, r_c=2.5 σ
K	Spring constant of FENE bond, K=30	T	Heat bath, T=1.1
R_0	Finite extensibility of FENE bond	Random number	881488529

Table 1. Parameters in the simulation and some of their values. (All these value are with reduced Lenard Jones units.)

Chapter 4: Results and Discussion

4.1 Initial State

Initially, we put only PS particles in the lattice site, like figure 1a. PCBM particles was then insert by dissociating some of PS chain and altering them into PCBM. The particles interacted via the potentials mentioned above. When system achieved equilibrium state we dissociate 20% percent of PS and alter them to P3HT. So the volume fraction is 1:4 for P3HT:PS, and fraction of PCBM varies in the study.

Most of our work start from the phase that P3HT chains randomly distributed in simulation box, see figure 18. PS particles were made transparent, through the entire context, in order to observe inner structure more clearly.

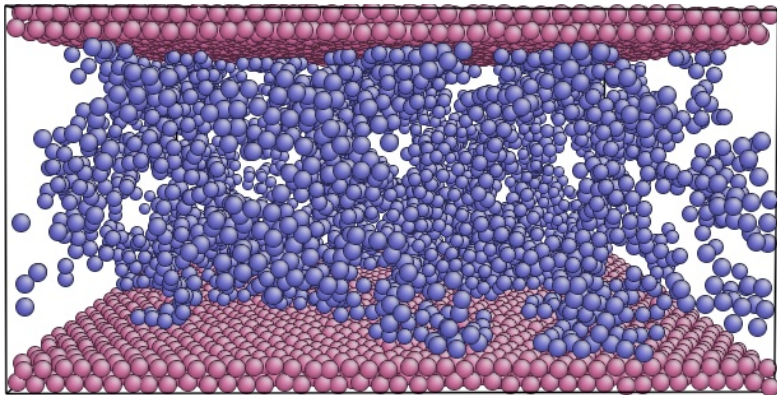

Figure 18. Random distributed P3HT chains (blue color) in simulation box. Walls are pink color one, PS was made transparent, and there is no PCBM in this system.

4.2 Formation of Column Structure

Starting from the initial condition in figure 19, we start our work to study the aggregation of P3HT in presence of PS. Phase separation was enabled by set δ between

P3HT and PS less than one as mentioned above. We simulate the system for millions steps and keep tracking the structure of P3HT phase, figure 19 shows the time evolution of the phase structure with δ set 0.75.

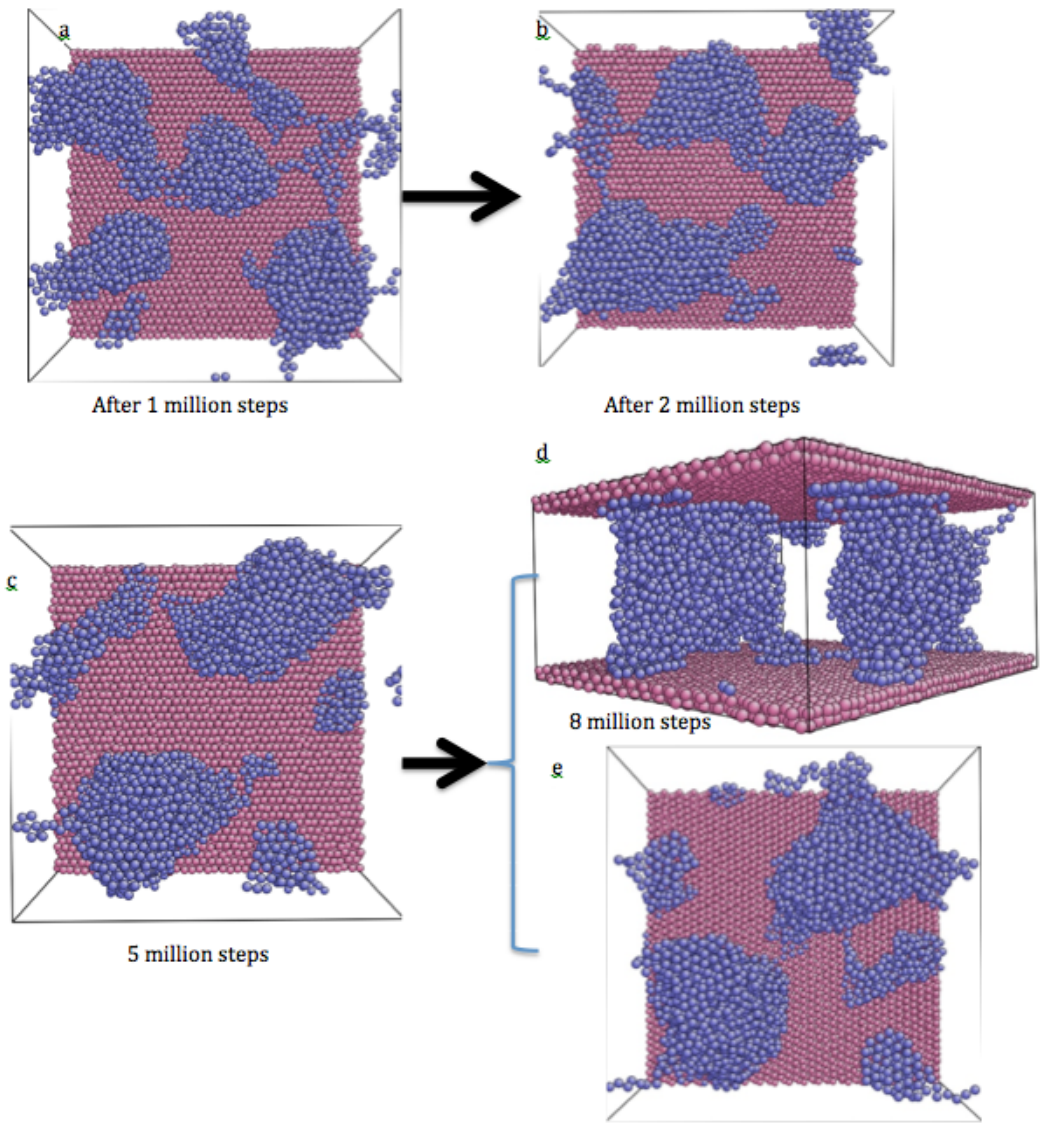

Figure 19. Structures of P3HT phase at different stage. (a) Structure after 1 million steps. (b) Structure after 2 million steps. (c) Structure after 5 million steps. (d) and (e) are Structure after 8 million steps with different angle of view.

It was observed, randomly distributed P3HT soon aggregated and formed bulk phase. With more simulation time, the bulks aggregate with each other and finally formed stable column structure that span between the top and bottom walls. This formation can be explained that since we set δ=0.75 between P3HT and PS, thus the force between them was dominated by repulsion. This simulates the incompatible nature of P3HT and PS. To reduce the mix free energy ΔG_{mix}, the system naturally tended to decrease interfacial energy by reducing interface area. Bulk aggregation was common phenomenon that happens when nano-scale particles was distribute in heterophilic solvents. This phenomenon also applied to our P3HT and PS blends. Since P3HT also interact with wall particles, contacting with walls could also reduce interfacial area. The column structure we predicted matches well with experiment results achieved by Miriam Rafailovich and her students. The TEM pictures from top view 20a and the vertical view, 20b, by looking at cross-section of the thin film indicated the phase seperation of P3HT bulk and PS, while from the cross-section picture, a column structure through top and bottom edges was clearly shown.

a

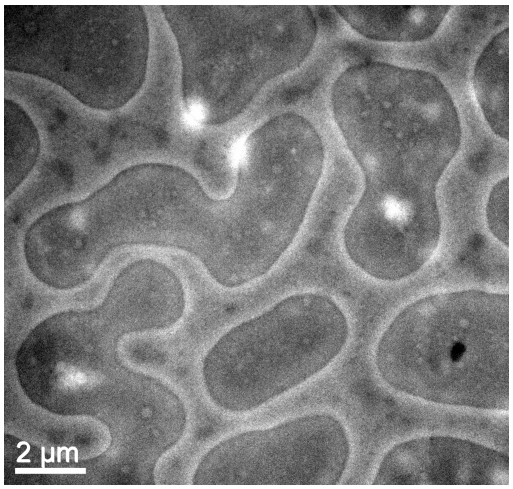

b

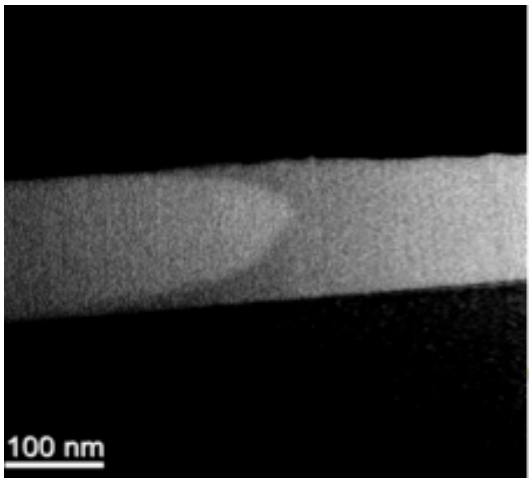

Figure 20. (a) TEM picture of PS:P3HT:PCBM 1:1:1 thin film, top view. (b) TEM picture of the cross-section.

4.3 Impact of δ on Phase Structure

The phase separation was driven by interfacial energy and was controlled by the value of δ in our simulation. Smaller δ value means the pairs are more mutually exclusive. Impact of δ on interaction force has been talked in figure 21. We launched simulation of systems with different value of δ while the starting states were same as in figure 18. The structures of these simulations after 8 million steps were shown in figure 21.

These pictures proves again that column structure could be self organized in P3HT:PS blends. Meanwhile, with same simulation steps, the system with smaller δ=0.55 has only 1 column structure in the simulation box, in contrast, other systems have 2 columns. It also can be observed, with same simulation steps, systems with larger δ have more isolated bulks. (figure 21c and 21d, those small bulks besides columns). Although the structure might have been affected by the limited size of our simulation ensemble. It is

still sufficient to conclude that δ value (which is correlated to interfacial energy) could affect the speed and degree of aggregation.

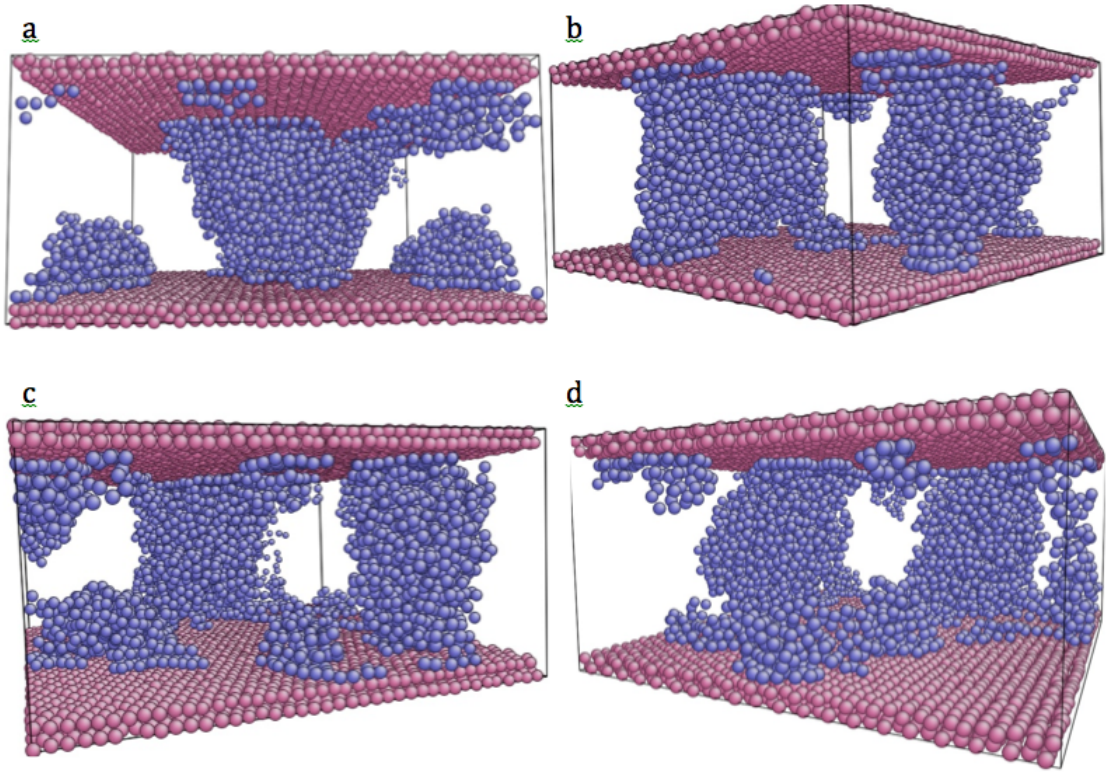

Figure 21. Structures of systems with different δ value, after 8 million simulation steps. (a) δ=0.55. (b) δ=0.75 (c) δ=0.85 (d) δ=0.95.

To strengthen our prediction, we continued the system with δ＝0.75 for another 8 million steps, the result was shown in figure 22. With additional simulation time, 2 columns structure was shown to aggregate into only 1 structure. This can be explained that 1 column, in geometry, has smaller area compare to 2 column with same volume, thus the change obeys the rule of free energy minimization by reduce the interfacial area of two heterophilic species. However, in our simulation systems, we find that even with

same initial condition, result structure can be either with 1 column or with 2 column, thus the number of columns seems like a random selection. But if we think over the situation in real thin film system, this event is quiet straight forward. Since the column structures in thin film have sizes from several nanometers to tenth nanometers, our simulation box can only contain 1 big column or 2 relatively smaller ones.

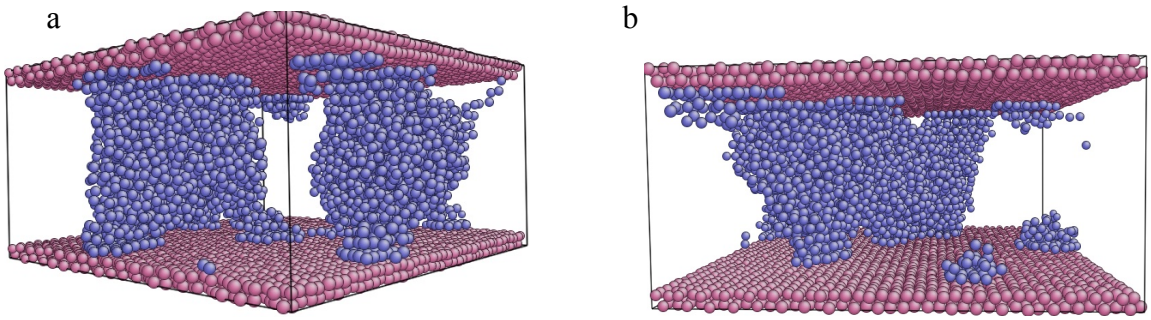

Figure 22. Structures evolved with time from (a) 8 million steps to (b) 16 million steps.

We also track the number of P3HT particles that locate at the interface through simulation*, see figure 23. This number was propotional to interface area, $S_{interface} \sim N$ (number of particles at interface). Along with simulation time, interface area keeps decreasing. At same simulation steps, larger repulsion between P3HT and PS lead to smaller interface area, which is a more stable state.

Number

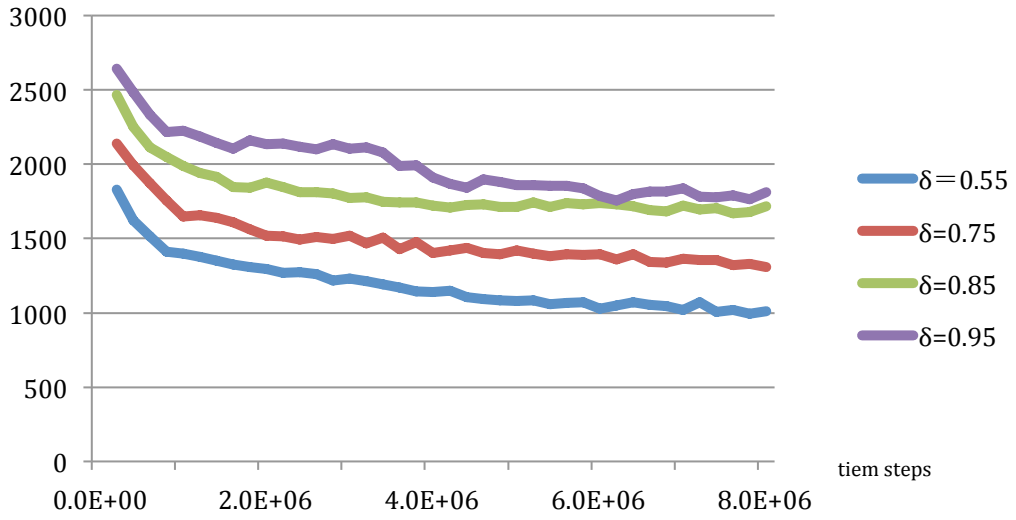

Figure 23. Number of P3HT particles at interface along with time steps. In all 3456 P3HT particles were in the simulation box.

* The number of P3HT particles at interface was roughly estimated by calculating the distance to nearest PS particles. If the distance is within the range of 1.6σ, we considered it as at interface.

4.4 Nanofiller Confinement

PCBM was acceptor material in a P3HT:PCBM photovoltaic device. It has been talked that PCBM phase should contact with P3HT to enable exciton dissociation. In PS:P3HT blend, since PS and P3HT particles are mutually exclusive, third party Nano-fillers will tend to locate at PS:P3HT interface to reduce the repulsion force between them. Here we studied the impact of some parameters to the confinement of PCBM. The parameters include fraction of PCBM, the repulsion force between P3HT and PS (δ value), and compatibility of PCBM to PS and P3HT.

Firstly, we investigate the impact of PS:P3HT miscibility on the confinements of PCBM by varying δ between PS and P3HT. We put 64 PCBM particles into the box and made it neutral to PS and P3HT ($\delta_{P3HT:PCBM}$=1.0, $\delta_{PS:PCBM}$=1.0), all other parameters were set the same for parallel comparison. The positioning of PCBM and structure of P3HT, after 5 million time steps, was shown in figure 24. It is shown when $\delta_{P3HT:PS}$=0.75, there are particles distributed in places other than interface (green arrow). In contrast, if $\delta_{P3HT:PS}$=0.55, most of the 64 PCBM particles were locate at the interface of P3HT and PS.

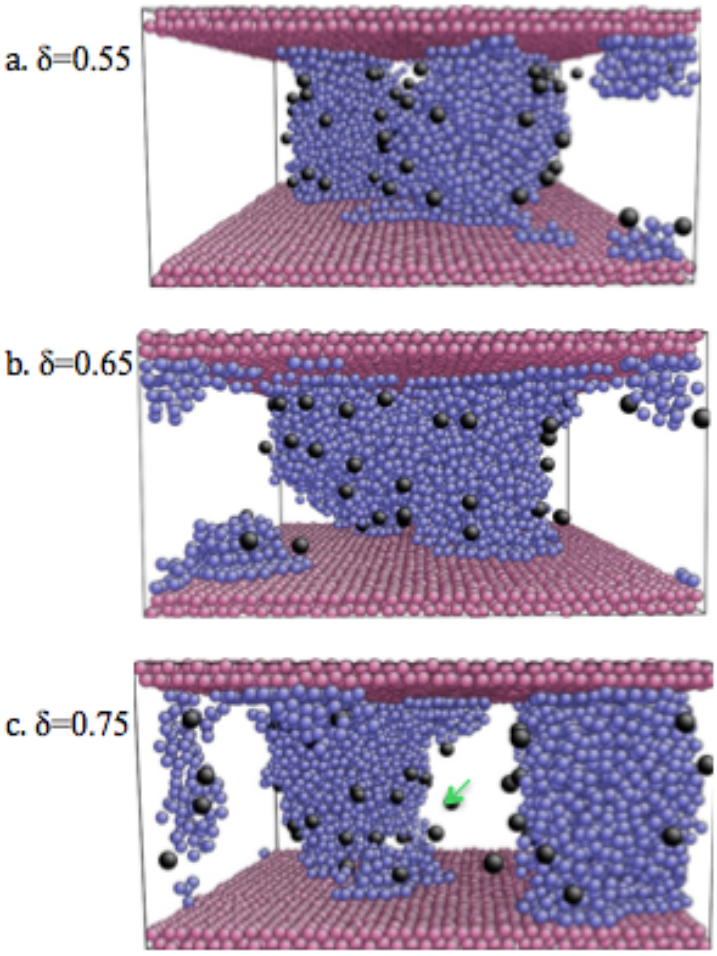

Figure 24. Position of PCBM (black) and structure of P3HT (blue) in simulation systems after 5 million steps. (a) $\delta_{P3HT:PS}$=0.55. (b) $\delta_{P3HT:PS}$=0.65. (c) $\delta_{P3HT:PS}$=0.75

We also calculate the number of PCBM particles that at the interface along with simulating time, figure 25. From the results, we can conclude that when P3HT and PS are more immiscible ($\delta_{P3HT:PS}$ smaller), PCBM particles will have higher concentration at interface due to high driven force from interfacial energy.

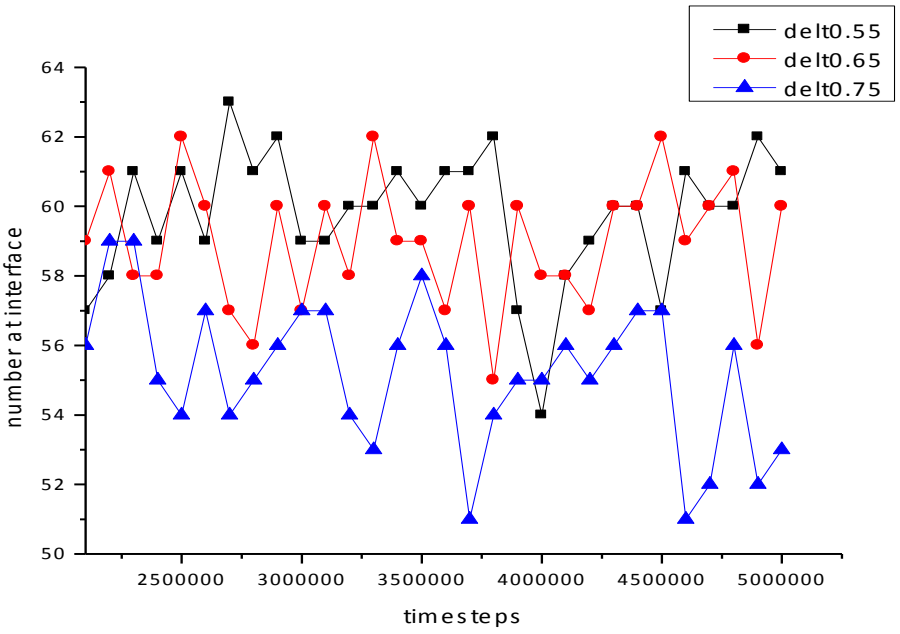

Figure 25. Number of PCBM at interface alone with simulation time for different degree of immiscibility between PS and P3HT.

The confinement of PCBM was driven by the repulsion of PS and P3HT. However, interaction between itself and other two particles should also affect the distribution. In an experiment study, it was found that in a bilayer of P3HT and PS thin film, PCBM would concentrate mostly in the interface plane, however, some diffused into P3HT phase. To adjust our parameters to better fit the realistic, we designed a bilayer

in our simulation and put 256 PCBM particles into it. By making PCBM neutral or repulsive to PS ($\delta_{PCBM:PS}$ less than 1.0), we get different results, shown in figure 26. When PCBM was neutral to PS or P3HT, though PCBM have highest concentration at interface. A large amount of it random distribute in PS and P3HT phase. If make PCBM slightly repulsive to PS ($\delta_{PCBM:PS}$=0.95), very few PCBM will be found in PS phase and more will be locate at interface. If $\delta_{PCBM:PS}$ further decrease (to 0.80 in figure 23d), PCBM particles tended to randomly distribute in P3HT phase rather than confined at interface.

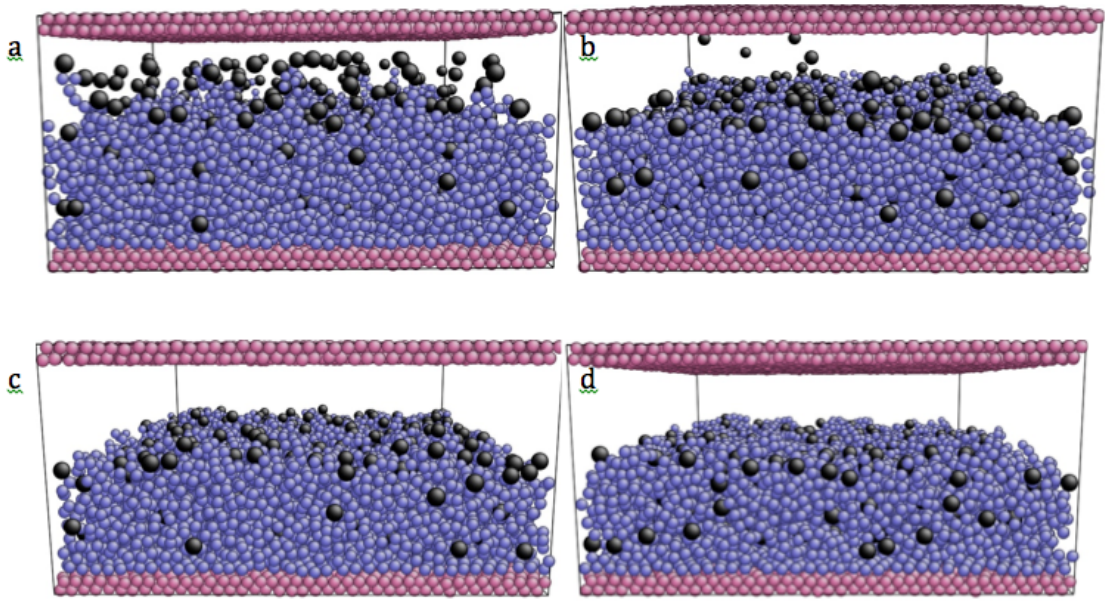

Figure 26. Distribution of PCBM in P3HT:PS bilayer after 3 million steps. (PS was made transparent) a. $\delta_{PCBM:PS}$=1.0 (neutral); b. $\delta_{PCBM:PS}$=0.95; c. $\delta_{PCBM:PS}$=0.90; $\delta_{PCBM:PS}$=0.80.

We then choose $\delta_{PCBM:PS}$=0.90 and investigate systems with different fraction of PCBM. Shown in figure 27 are structures after 8 million steps with number of PCBM particles equal 64, 256, 512, 1024 respectively (16384 particles of entire simulation box)

Or, in volume fraction (PCBM:P3HT) at 1:15, 4:15, 8:15 and 16:15 respectively. We can see from figure 27 that most of PCBM particles concentrated at interface when the fraction is low, however, if the fraction increase to certain degree, P3HT:PS interface can not afford enough space and thus lead to a random distribution of P3HT.

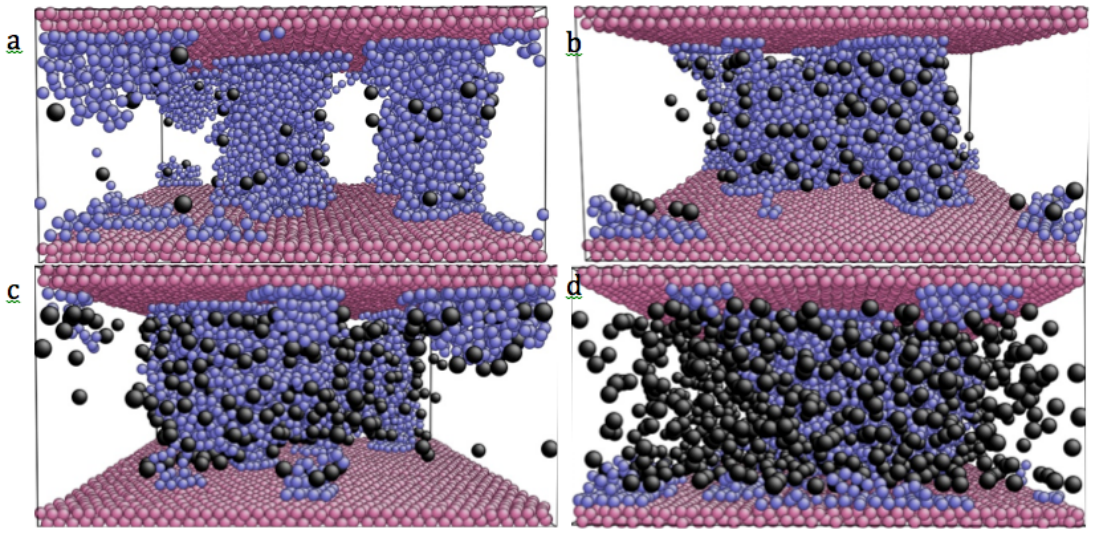

Figure 27. Systems with different number of PCBM particles (after 8 million steps). From a to d, number of PCBM equal 64, 256, 512, and 1024 respectively.

Chapter 5: Conclusion

We used Molecular dynamic simulation to investigate the morphology of P3HT:PS:PCBM blends. Our results strengthened the experimental discovery of P3HT column structure in P3HT:PS:PCBM thin film and revealed the effects of some parameter to the structure.

We have proved that two immiscible species (P3HT:PS) could self organized into column structure in a thin film device and the column was vertically through the thin film by contacting two electrodes. The self-organizing was driven by interfacial energy between the two species (P3HT and PS), and the structure evolves with time while moving toward more stable phase that with smaller interface area. This relate to experiments that processing time could lead to different nano structure of thin film while using this type of self-assembly technique. We have also revealed that difference in repulsion force could affect the speed of self-assembly and lead to different level of aggregation. Thus when the choice of polymer and surface modification would be a very important factor of morphology.

We further studied when third party particles (PCBM) was added to the blends, PCBM will move to the interface in order to reduce the repulsion between P3HT and PS. However, the positioning of PCBM was sensitive to interaction forces in the system. Larger repulsion force between P3HT and PS could drive more PCBM to be located at interface. If PCBM was made slightly repulsive to PS, it will results a distribution of PCBM that mostly locate at interface and some will diffused into P3HT phase. We also find the area of interface between PS and P3HT would limit the locating of PCBM at

interface. When P3HT:PS interface was fully occupied by PCBM, rest of them will be randomly distributed.

Our work explained the underlying theories of a column structure self-assembly process. The results could provide guidance to experimental study of morphology control in thin film processing.

References

1. Bequerel E. Recherches sur les effects de la radiation chimique de la lumiere solaire, au moyen des courants electriques. *C.R. Acad. Sci*. 9: 145-149, 1839.

2. Martin A. Green. Third generation photovoltaics: solar cells for 2020 and beyond. Physica E 14: 65-70, 2002.

3. Chapin D.M. Fuller C.S. and Pearson G.L. A New Silicon p-n Junction Photocell for Converting Solar Radiation into Electrical Power. *J.Appl.Phys*. 25: 676-677, 1954.

4. Jenny Nelson. *The Physics of Solar Cells*, Imperial College Press, 2003, Chapter 1: p. 1-16.

5. Ge, Weihao. An overview of P3HT:PCBM, the most efficient organic solar cell material so far. *Solid State Physics* 1: 1-11, 2009.

6. Bruton, T.M, Luthardt G, Rasch, K.D, Roy K, Dorrity I.A, Garrard B, Teale L, Alonso J, Ulgalde U, Declerq K, Nijs J, Szlufcik J, Rauber A, Wettling W, Vallera A. A study of the manufacture at 500 MWp p.a. of crystalline silicon photovoltaic modules. *14th European Photovoltaic Solar Energy Conference*, Barcelona, 11–16, 1997.

7. A. Shah, P. Torres, R. Tscharner, N. Wyrsch, and H. Keppner. Photovoltaic Technology: The Case for Thin-Film Solar Cells. *Science* 285: 692-698, 1999.

8. Travis L. Benanti and D. Vekataraman. Organic solar cells: am overview focusing on active layer morphology. *Photosynthesis Research* 87: 73-81. 2006.

9. Hoppe, H. Sariciftci and N.S. Organic solar cells: An overview. *J. Mater. Res.*19: 1924-1945, 2004.

10. Fan Yang, Max Shtein, and Stephen R. Forrest. Controlled growth of a molecular bulk heterojunction photovoltaic cell. *Nature Materials* 4: 37-41, 2005.

11. Yu, G, Heeger, A. J, Hummelen J.C, Wudl F. Polymer Photovoltaic Cells: Enhanced Efficiencies via a Network of Internal Donor-Acceptor Heterojunctions. *J. Appl. Phys 270:* 1789-1791, 1995.

12. Halls J. J. M, Walsh C.A, Greenham N.C, Marseglia, E. A, Friend R.H, Moratti S.C, and Holmes A.B. Efficient photodiodes from interpenetrating polymer networks *Nature* 376: 498-500, 2002.

13. F. Padinger, R.S. Rittberger and N.S. Sariciftci. Effects of postproduction treatment on plastic solar cells. *Adv. Func. Mat.* 13: 85-88, 2003.

14. C.J. Brabec, Organic photovoltaics: Technology and market. *Solar Energy Materials and Solar Cells* 83: 273-292, 2004.

15. Gilles Dennler, Markus C. Scharber and Christoph J. Brabec. Polymer-Fullerene Bulk-Heterojunction Solar Cells. *Adv. Mater*. 21: 1323-1338, 2009.

16. Markus C. Scharber, David Mühlbacher, Markus Koppe, Patrick Denk, Christoph Waldauf, Alan J. Heeger, and Christoph J. Brabec. Design Rules for Donors in Bulk-Heterojunction Solar Cells—Towards 10 % Energy-Conversion Efficiency. *Adv. Mat*. 18: 789-794, 2006.

17. E. Bundgaard and F. C. Krebs. Low band gap polymers for organic photovoltaics. *Sol. Energy Mater. Sol. Cells* 91: 954–985, 2007.

18. Z. Zhu, D. Waller, R. Gaudiana, M. Morana, D. Muhlbacher, M. Scharber and C. Brabec. Panchromatic Conjugated Polymers Containing Alternating Donor/Acceptor Units for Photovoltaic Applications. *Macromolecules* 40: 1981–1986, 2007.

19. Xiaoniu Yang, Joachim Loos. Toward High-performance Polymer Solar cell – the importance of Morphology Control. *Macromolecules* 40: 1353-1362, 2007.

20. R. Palacios, P. Formentín, T. Trifonov, M. Estrada, R. Alcubilla, J. Pallarés1, and L. F. Marsal. Semiconducting P3HT microstructures: fibres and tubes obtained from macroporous silicon template. *Physica Status Solidi* 2: 206-208, 2008.

21. Jae Hyun Lee, Dae Woo Kim, Hong Jang, Jong Kil Choi, Jianxin Geng, Jae Wook Jung, Sung Cheol Yoon, and Hee-Tae Jung. Enhanced solar-cell efficiency in bulk-heterojunction polymer systems obtained by nanoimprinting with commercially available AAO membrane filters. *Small* 5: 2139-2143, 2009.

22. Xiaoniu Yang, Joachim Loos, Sjoerd C. Veenstra, Wiljan J. H. Verhees, Martijn M. Wienk, Jan M. Kroon, Matthias A. J. Michels, and René A. J. Janssen. Nanoscale Morphology of High-Performance Polymer Solar Cells. *Nano Lett* 5: 579-583, 2005.

23. J. Peet, J. Y. Kim, N. E. Coates, W. L. Ma, D. Moses, A. J. Heeger & G. C. Bazan. Efficiency enhancement in low-bandgap polymer solar cells by processing with alkane dithiols. *Nature Material* 6: 497-500, 2007.

24. Mariano Campoy-Quiles, Toby Ferenczi, Tiziano Agostinelli, Pablo G. Etchegoin, Youngkyoo Kim, Thomas D. Anthopoulos, Paul N. Stavrinou1, Donal D. C. Bradley, and Jenny Nelson. Morphology evolution via self-organization and lateral and vertical diffusion in polymer:fullerene solar cell blends. *Nature Material* 7: 158-164, 2008.

25. Katsuhiko Ariga, Jonathan P Hill, Michael V Lee, Ajayan Vinu, Richard Charvet and Somobrata Acharya. Challenges and breakthroughs in recent research on self-assembly. *Sci. Technol. Adv. Mater.* 9: 14-109, 2008.

26. Gavin A Buxton and Nigel Clarke. Computer simulation of polymer solar cells. *Modeling Simul. Mater. Sci. Eng.* 15: 3-26, 2005.

27. Jarvist M. Frost, Fabien Cheynis, Sachetan M. Tuladhar, and Jenny Nelson. Influence of polymer blend morphology on charge transport and photocurrent generation in Donor-Acceptor Polymer Blends. *Nano Letters* 6: 1674-1681, 2006.

28. Florent Monestier, Jean-Jacques Simon, , Philippe Torchio, Ludovic Escoubas, Franc- ois Flory, Sandrine Bailly, Remi de Bettignies, Stephane Guillerez, Christophe Defranoux. Modeling the short-circuit current density of polymer solar cells based on P3HT:PCBM blend. *Solar Energy Materials & Solar Cells* 91: 405-410, 2007.

29. Lingyi Meng, et al. Dynamic Monte Carlo Simulation for Highly Efficient Polymer Blend Photovoltaics. *J. Phys. Chem. B* 114: 36-41, 2010.

30. Lingyi Meng, Yuan Shang, Qikai Li, Yongfang Li, Xiaowei Zhan, Zhigang Shuai, Robin G. E. Kimber, and Alison B. Walker. Dynamical Monte Carlo Modelling of Organic Solar Cells: The Dependence of internal Quantum Efficiency on Morphology. *Nano Letters* 5: 1814-1818, 2005.

31. Chakravarthy Ayyagari. A molecular dynamics simulation study of the influence of free surface on the morphology of self-associating polymers. *Polymer* 45: 4549-4558, 2004.

32. Pramod Kulkarni and Pratim Biswas. A Brownian Dynamics Simulation to Predict Mophology of Nanoparticle Deposits in the Presence of Interparticle interaction. *Aerosol Science and Technology* 38: 541-554, 2004.

33. Olaf Lenz. 12-6 Lennard-Jones Potential. Wiki cyclopedia (online accessed May 6th, 2012). http://en.wikipedia.org/wiki/File:12-6-Lennard-Jones-Potential.svg.

34. Kurt Kremer and Gary S. Grest. Dynamics of entangled linear polymer melts: A molecular-dynamic simulation. *J. Chem. Phys* 92: 5057-5086, 1990.

35. G. W. Gear. *Numerical initial value problems in ordinary differential equations*. Prentice-Hall, Englewook Cliffs, 1971.